Prediction, Detection, and Correction of Faraday Rotation in Full-Polarimetric L-Band SAR Data

Franz J. Meyer, *Member, IEEE*, and Jeremy B. Nicoll

***Abstract*—With the synthetic aperture radar (SAR) sensor PALSAR onboard the Advanced Land Observing Satellite, a new full-polarimetric spaceborne L-band SAR instrument has been launched into orbit. At L-band, Faraday rotation (FR) can reach significant values, degrading the quality of the received SAR data. One-way rotations exceeding 25° are likely to happen during the lifetime of PALSAR, which will significantly reduce the accuracy of geophysical parameter recovery if uncorrected. Therefore, the estimation and correction of FR effects is a prerequisite for data quality and continuity. In this paper, methods for estimating FR are presented and analyzed. The first unambiguous detection of FR in SAR data is presented. A set of real data examples indicates the quality and sensitivity of FR estimation from PALSAR data, allowing the measurement of FR with high precision in areas where such measurements were previously inaccessible. In examples, we present the detection of kilometer-scale ionospheric disturbances, a spatial scale that is not detectable by ground-based GPS measurements. An FR prediction method is presented and validated. Approaches to correct for the estimated FR effects are applied, and their effectiveness is tested on real data.**

***Index Terms*—Faraday rotation (FR) correction, FR estimation, ionospheric effects, L-band synthetic aperture radar (SAR).**

I. Introduction

AT L-BAND, the ionosphere is assumed to have considerable effects on synthetic aperture radar (SAR), Interferometric SAR (InSAR), and SAR polarimetry. Range shifts, internal image deformations, range and azimuth blurring in SAR images, azimuth streaking in interferograms, interferometric phase errors, and Faraday rotation (FR) are the most prominent. PALSAR images can serve as an important data source to both investigate ionospheric effects on SAR and demonstrate that they can be corrected.

While the origin and extent of ionospheric effects on SAR image quality and SAR interferometry are published in, e.g., [1]–[6], this paper focuses on the issue of FR, which is a rotation of the polarization vector of radio waves that propagated through the ionosphere. Anisotropy in the ionosphere due to charged particles in the presence of a persistent magnetic field causes this rotation [7]. Linearly polarized SAR data quality can be significantly impacted if the effect is not corrected [1], [8], [9]. FR effects can hamper or complicate calibration efforts, where FR can mask crosstalk between polarization channels. FR angles of less than 5° were established as acceptable for a number of commonly used parameter extraction methods from SAR data [10]. Higher FR levels may cause significant errors in SAR image interpretation and data analysis, particularly decompositions relying on channel ratios.

FR is frequency dependent and is expected to be much more severe for L-band than for C-band under the same ionospheric conditions [10]. However, the extent of FR effects on the backscatter signature for a spaceborne L-band polarimetric instrument is not well known experimentally, due to a lack of data. With the recent (January 2006) launch of the Japan Aerospace Exploration Agency's (JAXA's) Advanced Land Observing Satellite (ALOS) PALSAR mission, a rich archive of L-band SAR data is becoming available.

One of the potential limitations to using this data set is the difficulty in detecting and correcting for FR, particularly for dual- and single-polarization data. A listing of estimated FR for all PALSAR image frames could greatly aid in data selection for researchers wishing to avoid FR effects or for those deliberately investigating these effects. In Sections II and III, methods and examples for detecting FR effects in fully polarized data sets are presented. In Section IV, an approach for correcting FR effects is applied and tested on real data. A performance discussion and an outlook finalize this paper.

II. Detection of FR in Full-Pol SAR Data

A. Physical Background

In the ionosphere, highly energetic solar radiation leads to the ionization of some atmospheric molecules and creates a mixture of free electrons, ions, and neutral gases. The density of free electrons n_e is a function of the sun's activity, the atmospheric density profile, the geographic location, the magnitude and orientation of the Earth's magnetic field, and the time of day.

The effect of the ionosphere on electromagnetic signals is described by the Appleton–Hartree equation that relates the refractive index of a medium to its state of ionization. For SAR systems, which operate well above the ionosphere's plasma frequency, the Appleton–Hartree equation can be approximated by [11]

$$n \approx 1 - \frac{1}{2}\frac{f_{\mathrm{N}}^2}{f^2}\left(1 \mp \frac{f_{\mathrm{H}}}{f}\cos(\theta)\right) - \frac{1}{8}\frac{f_{\mathrm{N}}^4}{f^4} + \cdots \qquad (1)$$

with signal frequency f, the angle between the magnetic field and the signal propagation θ, electron gyrofrequency $f_{\mathrm{H}} = B \cdot e/2\pi \cdot m$, plasma frequency $f_{\mathrm{N}} = \sqrt{n_e e^2/4\pi^2\varepsilon_0 m}$, electron charge e, electron mass m, the dielectric permittivity ε_0, and the local geomagnetic field B. The deviation of the refraction index

Manuscript received August 23, 2007; revised March 17, 2008 and May 29, 2008. Current version published October 1, 2008.

The authors are with the Alaska Satellite Facility, University of Alaska Fairbanks, Fairbanks, AK 99775 USA (e-mail: fmeyer@asf.alaska.edu; jnicoll@asf.alaska.edu).

Digital Object Identifier 10.1109/TGRS.2008.2003002

in the ionosphere from unity is small under normal atmospheric conditions; thus, the scaled-up "refractivity" N_{iono} is often used instead of n, i.e., $N_{\mathrm{iono}} = (n-1)\cdot 10^6$.

For signals propagating vertically through the ionosphere, the first and most significant term of (1) causes a phase shift that can be obtained by integrating N_{iono} from the top of the ionosphere along the (one way) ray path to the ground

$$\phi(f) = -2\pi f \frac{1}{10^6}\int \frac{N_{\mathrm{iono}}(f,h)}{c}dh \approx 2\pi\frac{K}{cf}\mathrm{TEC} \quad (2)$$

where $\mathrm{TEC} = \int N_{\mathrm{iono}}(f,h)dh$ is the ionospheric *total electron content* (TEC) integrated along the vertical, and $K = 1/2\cdot e/(4\pi^2 m\varepsilon_0) = 40.28\ [\mathrm{m}^3/\mathrm{s}^2]$.

The $\mp$ in the second summand of (1) expresses the different propagation velocities of left- and right-handed signals in the ionosphere, causing a phase difference between these polarizations, which is a phenomenon known as FR [1]. Following (1), the magnitude of FR for a wave of frequency f that has traveled vertically one way through the ionosphere is given by

$$\Omega = \phi(f)\cdot\frac{f_h}{f}\cos(\theta) = -2\pi f\frac{1}{10^6}\int\frac{N_{\mathrm{iono}}(f,h)}{c}\frac{f_h}{f}\cos(\theta)dh$$
$$= \frac{K}{f^2}B\cos(\theta)\mathrm{TEC}. \quad (3)$$

Equations (2) and (3) indicate the dispersive nature of the ionosphere, as both phase delay and FR effects scale with frequency. They also show that the actual distribution of electrons along the ray path is not significant, i.e., if TEC is known, both the phase delay and the FR can be determined. Higher order terms of (1) are insignificant for SAR operating above 250 MHz and are neglected in this paper.

As SAR sensors observe the Earth in an oblique geometry, (3) has to be projected into the slant signal path using mapping functions. To develop a mapping function M, an idealized single-layer approximation of the ionosphere is often applied. In this approximation, the altitude at which a ray between the satellite and the Earth's surface pierces the layer with maximal electron density is defined as the effective ionospheric height h_{sp}. In this study, $h_{\mathrm{sp}} = 400$ km is assumed [8]. The projection of this point on the ground is labeled *subionospheric point* P_{sp}. To calculate the mapping function, the zenith angle χ of the rays at the subionospheric point at height h_{sp} is needed. The mapping function is then given by

$$M = \frac{1}{\cos(\chi)} \quad (4)$$

where the cosine of the zenith angle can be approximated by

$$\cos(\chi) = \sqrt{1-\left(\frac{R_{\mathrm{e}}\cos(\varepsilon)}{R_{\mathrm{e}}+h_{\mathrm{sp}}}\right)^2} \quad (5)$$

with the Earth radius R_{e} and the elevation angle relative to the horizon ε. A spherical Earth is assumed in (5).

Equation (4) can be approximated by $M = \sec(\varphi)$, where φ is the off-nadir look angle of the SAR. The error introduced by this approximation is less than 10% for $\varphi \le 48^\circ$ and, therefore, sufficient for many purposes. By considering (1)–(5), the *(one-way) FR* inherent in SAR data of frequency f corresponds to [8]

$$\Omega = (K/f^2)\int_0^{\mathrm{h}} n_e B\cos(\theta)\frac{1}{\cos(\chi)}dh$$
$$\approx (K/f^2)B\cos(\theta)\sec(\varphi)\mathrm{TEC}. \quad (6)$$

B. FR Prediction

1) Prediction Method: Based on (6), FR angles in low-frequency spaceborne SAR data can be predicted. Equation (6) shows that screening the archive simply by using ionospheric TEC maps is insufficient for finding high FR events. A model for predicting FR, taking both the geometries between the magnetic field and the satellite pointing angles as well as the ionospheric activity into account, was successfully employed to find fully polarimetric data sets with relatively high FR for this paper. In its main features, the implemented approach follows a method published in [8]. However, instead of a generic satellite configuration, the real observation geometry of all PALSAR images archived in the American ALOS Data Node (AADN) was used for a detailed granule-by-granule FR prediction.

Vertical TEC values, necessary for evaluating (6), are derived from global ionosphere maps (GIMs) that are generated on a daily basis at the Center for Orbit Determination in Europe (CODE), using data from about 150 GPS sites of the International GNSS service and other institutions. TEC is modeled in a solar-geomagnetic reference frame using a spherical harmonics expansion up to degree and order 15. The time spacing between maps is 2 h, and each map consists of a grid of values spaced at 2.5° latitude and 5° longitude. Data were downloaded from http://aiuws.unibe.ch/ionosphere/. The accuracy of the TEC maps is best over areas with denser GPS or station coverage and worst over areas such as the ocean where the coverage is minimal, but it is still generally considered to be within 5×10^{16} electrons/m^2 [12]. Latitude-dependent relative standard deviations of TEC maps were estimated from a comparison of CODE model results with JASON dual-frequency altimeter TEC [13]. CODE TEC results are comparable with those from other sources (e.g., [14]), and a change of model does not significantly affect FR prediction. Due to the low resolution of the used TEC maps, the position of the subionospheric point P_{sp} is approximated with the coordinates of the scene center in the prediction approach.

The geomagnetic field used for FR prediction was calculated from geomagnetic data provided by the National Geophysical Data Center (http://www.ngdc.noaa.gov/), based on the International Geomagnetic Reference Field [15]. The standard deviation of the measurements is specified to be about 250 nT [15]. Calculations were generated at 1° increments in latitude and longitude for late Fall 2006.

The off-nadir angle φ and the angle θ between the magnetic field and the satellite pointing were derived from PALSAR catalog metadata, located at the Alaska Satellite Facility's (ASF's) AADN. Pointing angles toward the image center were used to represent the observation geometry.

2) Error Budget of FR Prediction: The performance of FR prediction $\sigma_\Omega^{\mathrm{pr}}$ is defined by the quality of the input

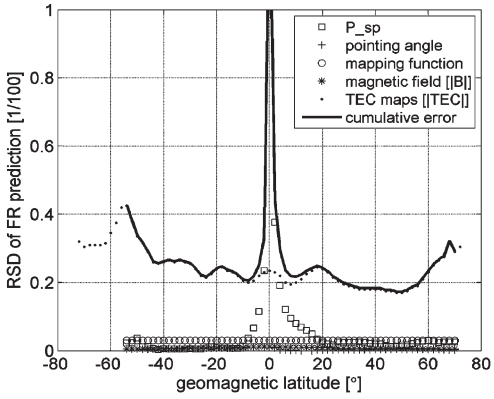

(a)

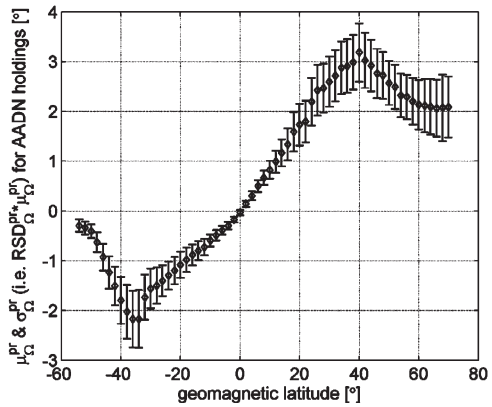

(b)

Fig. 1. Error budget of FR prediction as a function of geomagnetic latitude. (a) Relative standard deviation of predicted FR as a function of geomagnetic latitude. (b) Absolute errors of predicted FR ($\mathrm{RSD}_\Omega^{\mathrm{pr}} \cdot \Omega$) together with the mean FR in test data sets.

information needed for evaluating (6) and can be estimated via error propagation

$$\sigma_\Omega^{\mathrm{pr}} = \sqrt{\frac{\partial\Omega}{\partial B}\sigma_B^2 + \frac{\partial\Omega}{\partial\theta}\sigma_\theta^2 + \frac{\partial\Omega}{\partial\varphi}\sigma_\varphi^2 + \frac{\partial\Omega}{\partial\mathrm{TEC}}\sigma_{\mathrm{TEC}}^2 + \frac{\partial\Omega}{\partial P_{\mathrm{sp}}}\sigma_{P_{\mathrm{sp}}}^2} \tag{7}$$

where σ^2 is the variance of each of the error-contributing terms in (6). The first (σ_B^2) and the fourth $(\sigma_{\mathrm{TEC}}^2)$ terms can be solved analytically using information in Section II-B1. σ_θ^2, the error in the measurements of the angle between the pointing angle and the magnetic field, was solved numerically by substituting the near- and far-range look angles into the model and by taking the difference of the results as the error. σ_φ^2 is caused by approximating the mapping function by $M = \sec(\varphi)$. The error in P_{sp} results from assuming that the ionospheric center coincides with the center of the SAR scene.

Fig. 1 shows individual error contributions and cumulative errors of FR prediction as a function of geomagnetic latitude. As shown in Fig. 1(a), the relative standard deviation $(\mathrm{RSD}_\Omega^{\mathrm{pr}})$ of FR prediction is dominated by latitude-dependent errors in the GPS-derived TEC maps (cf. [13]). Sensor attitude and location uncertainties influence the error budget strongest in areas close to the geomagnetic equator, where angles between magnetic field lines and observation direction are almost orthogonal. At 0° geomagnetic latitude, the cumulative $\mathrm{RSD}_\Omega^{\mathrm{pr}}$ is infinite due to $\Omega = 0°$. The contribution of mapping function approximations, as well as uncertainties of magnitude and orientation of magnetic field lines, is negligible. Cumulative errors in FR prediction are between 20% and 40% $\mathrm{RSD}_\Omega^{\mathrm{pr}}$, except at the geomagnetic equator, where FR values approach zero. The absolute error of FR predictions is shown in Fig. 1(b), together with the latitude-dependent mean FR in the AADN holdings as of January 23, 2007. Absolute errors are calculated from $\sigma_\Omega^{\mathrm{pr}} = \mathrm{RSD}_\Omega^{\mathrm{pr}} \cdot \Omega$ and are depicted as error bars. A comparison of Fig. 1(a) and (b) shows that, while the best relative standard deviation is reached at moderate northern latitudes, the most precise results are from data at the geomagnetic equator. Note that absolute errors will increase with Ω, which is expected to rise to about 27° during the lifetime of PALSAR [8].

C. FR Estimation From SAR

In the presence of FR, the symmetry of the measured scattering matrix is violated $(\mathrm{HV} \neq \mathrm{VH})$. If full-polarimetric (full-pol) SAR data are available, this effect can be used to estimate FR from the data by comparing the cross-polarized (cross-pol) terms of the scattering matrix. According to Freeman [16], the measured scattering matrix M of a SAR system measuring linear horizontal (H) and vertical (V) polarized signals can be written as

$$M = Ae^{j\phi} R^T R_{\mathrm{F}} S R_{\mathrm{F}} T + N \tag{8}$$

where S is the scattering matrix, R_{F} corresponds to the one-way FR matrix, R and T are the receive and transmit distortion matrices, A represents the overall gain of the radar system, $e^{j\phi}$ corresponds to the round-trip phase delay, and N is an additive noise term. A more detailed description of (8) is as follows:

$$\begin{bmatrix} M_{\mathrm{hh}} & M_{\mathrm{hv}} \\ M_{\mathrm{vh}} & M_{\mathrm{vv}} \end{bmatrix} = Ae^{j\phi} \cdot \begin{bmatrix} 1 & \delta_1 \\ \delta_2 & f_1 \end{bmatrix}^{\mathrm{T}} \cdot \begin{bmatrix} \cos\Omega & \sin\Omega \\ -\sin\Omega & \cos\Omega \end{bmatrix} \cdot \begin{bmatrix} S_{\mathrm{hh}} & S_{\mathrm{hv}} \\ S_{\mathrm{vh}} & S_{\mathrm{vv}} \end{bmatrix} \cdot \begin{bmatrix} \cos\Omega & \sin\Omega \\ -\sin\Omega & \cos\Omega \end{bmatrix} \cdot \begin{bmatrix} 1 & \delta_3 \\ \delta_4 & f_2 \end{bmatrix} + \begin{bmatrix} N_{\mathrm{hh}} & N_{\mathrm{hv}} \\ N_{\mathrm{vh}} & N_{\mathrm{vv}} \end{bmatrix} \tag{9}$$

where the transmit and receive distortion matrices are expressed by the crosstalk factors $\delta_1, \ldots, \delta_4$, as well as the channel imbalance factors f_1 and f_2, of the transmit and receive antenna. The FR matrix is expressed by the FR angle Ω.

Based on recent studies of the calibration quality of ALOS PALSAR, the calibration techniques applied to PALSAR data can successfully estimate and largely correct for the system-dependent matrices A, R, and T. Channel imbalances are, in general, well compensated by using JAXA's distortion matrices. The residual amplitude imbalance is estimated to be between 0.5 and 1 dB, whereas the phase imbalance is within 1°–5° [17]. Published values for crosstalk vary from −25 dB (see [17]) to −45 dB (see [18]). The noise equivalent sigma zero (NESZ) is estimated to be about −27 dB. Within this paper, we will show that biases identified in FR estimates are consistent with theoretical biases caused by calibration errors as published in [17] and [18]. The limited range of FR values observed in the early stage of the PALSAR mission prevents a more detailed

diagnosis of calibration errors. However, with increasing variability of FR values at later mission stages, an analysis of FR estimation biases will allow more insight into the nature and size of calibration errors.

1) Estimation Methods: Assuming residual calibration errors can be ignored, and by disregarding uncompensated receiver noise, the scattering matrix M' of a calibrated image can be written as

$$\begin{bmatrix} M'_{\rm hh} & M'_{\rm vh} \\ M'_{\rm hv} & M'_{\rm vv} \end{bmatrix} = \begin{bmatrix} \cos\Omega & \sin\Omega \\ -\sin\Omega & \cos\Omega \end{bmatrix} \cdot \begin{bmatrix} S_{\rm hh} & S_{\rm vh} \\ S_{\rm hv} & S_{\rm vv} \end{bmatrix} \cdot \begin{bmatrix} \cos\Omega & \sin\Omega \\ -\sin\Omega & \cos\Omega \end{bmatrix}. \quad (10)$$

Nonzero FR causes the cross-pol measurements $M'_{\rm vh}$ and $M'_{\rm hv}$ to be nonreciprocal, an effect that can be exploited for FR retrieval. An estimate $\hat{\Omega}$ of the FR angle Ω can be derived by solving the equation system in (10) directly (see [16]), yielding

$$\hat{\Omega} = \frac{1}{2}\tan^{-1}\left[\frac{(M'_{\rm vh} - M'_{\rm hv})}{(M'_{\rm hh} + M'_{\rm vv})}\right]. \quad (11)$$

Equation (11) is based on scattering matrix data. Such measures are not susceptible to initial averaging of the scattering matrix and are affected by significant errors. Therefore, the approach in (11) will be disregarded in the remainder of this paper.

An improved FR estimation method based on covariance matrix data was proposed in [16] that uses averaged second-order statistics. From $Z_{\rm hv} = 0.5(M_{\rm vh} - M_{\rm hv})$, an estimate of Ω is derived

$$\hat{\Omega} = \pm\frac{1}{2}\tan^{-1} \times \left[\sqrt{\frac{4\langle Z_{\rm hv} Z^*_{\rm hv}\rangle}{(\langle M'_{\rm hh} M'^*_{\rm hh}\rangle + \langle M'_{\rm vv} M'^*_{\rm vv}\rangle + 2{\rm Re}\{\langle M'_{\rm hh} M'^*_{\rm vv}\rangle\})}}\right]. \quad (12)$$

A third FR estimation approach published in [19] applies a simple transformation of M' to a circular basis Z via

$$\begin{bmatrix} Z_{11} & Z_{12} \\ Z_{21} & Z_{22} \end{bmatrix} = \begin{bmatrix} 1 & j \\ j & 1 \end{bmatrix} \cdot \begin{bmatrix} M'_{\rm hh} & M'_{\rm vh} \\ M'_{\rm hv} & M'_{\rm vv} \end{bmatrix} \cdot \begin{bmatrix} 1 & j \\ j & 1 \end{bmatrix}. \quad (13)$$

From (13), an estimate for Ω can be derived by calculating

$$\hat{\Omega} = \frac{1}{4}\arg\left(Z_{12} Z^*_{21}\right). \quad (14)$$

2) Influence of Calibration Errors and Noise on FR Estimation: After statistical errors are removed by substantial spatial averaging, the quality of FR estimation is mainly affected by residual system noise, channel imbalance, and crosstalk. A concise and detailed sensitivity analysis of the FR estimation methods in (12) and (14), subject to a wide range of calibration errors and noise levels, is published in [16] for several surface types. This analysis shows that (14) is less sensitive to residual noise, channel imbalance, and crosstalk. Therefore, all further analyses will focus on (14).

Equations (9), (13), and (14) are employed to determine the performance of (14) subject to typical calibration errors in ALOS PALSAR data. As published values for the PALSAR calibration quality vary, best and worst case scenarios will be sketched, employing high and low calibration quality values, respectively. For convenience, $f_1 = f_2 = f$ and $\delta_1 = \delta_2 = \delta_3 = \delta_4 = \delta$ is assumed.

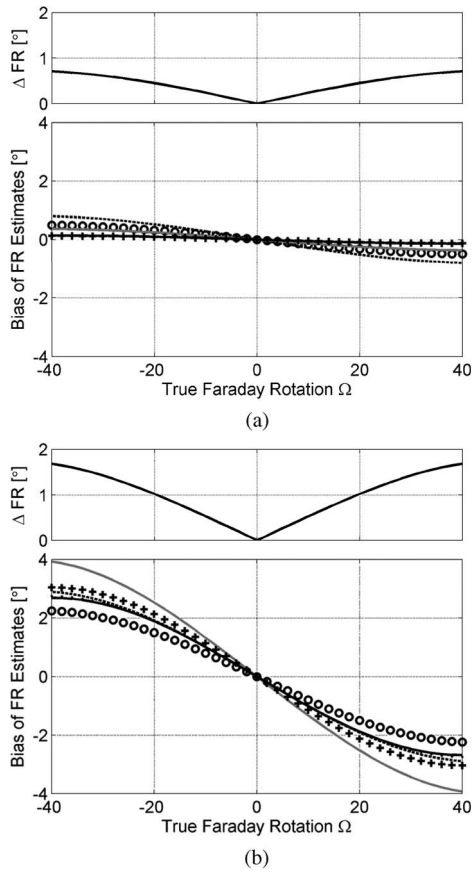

Fig. 2. Predicted biases of $\hat{\Omega}$ for several surface types (a) considering high calibration quality ($|f|^2 = 0.5$ dB, $\arg(f) = 1°$, and $|\delta|^2 = -45$ dB) and (b) considering low calibration quality ($|f|^2 = 1$ dB, $\arg(f) = 5°$, and $|\delta|^2 = -25$ dB). The NESZ is kept constant at -27 dB. Surface types include (dashed line) "bare soil," (o) "pasture," (gray solid line) "upland forest," $(+)$ "swamp forest," (black solid line) "plantation," and (.) "conifers."

In the presence of calibration errors, biases are introduced into the FR estimates. These biases depend on the type and magnitude of calibration errors, the real FR Ω, and the backscatter characteristics of the imaged surface. If natural terrain is observed, consisting of a mix of different surface types, target-dependent biases lead to a lateral variation of FR estimates $\hat{\Omega}$ throughout the image, even if the ionosphere is spatially homogeneous.

Fig. 2 shows the calibration-error-introduced biases of $\hat{\Omega}$ for several surface types considering high-end ($|f|^2 = 0.5$ dB, $\arg(f) = 1°$, $|\delta|^2 = -45$ dB, NESZ $= -27$ dB) and low-end ($|f|^2 = 1$ dB, $\arg(f) = 5°$, $|\delta|^2 = -25$ dB, NESZ $= -27$ dB) calibration qualities. Fig. 2(a) and (b) is composed of two subplots. The subplots in the lower part of Fig. 2 show FR biases as a function of true Ω for different surface types, including "bare soil" (dashed line), "pasture" (o), "upland forest" (gray solid line), "swamp forest" $(+)$, "plantation" (black solid line), and "conifers" (.). The top portion of the plots shows the spread of FR biases due to target-type dependence for every true FR angle Ω.

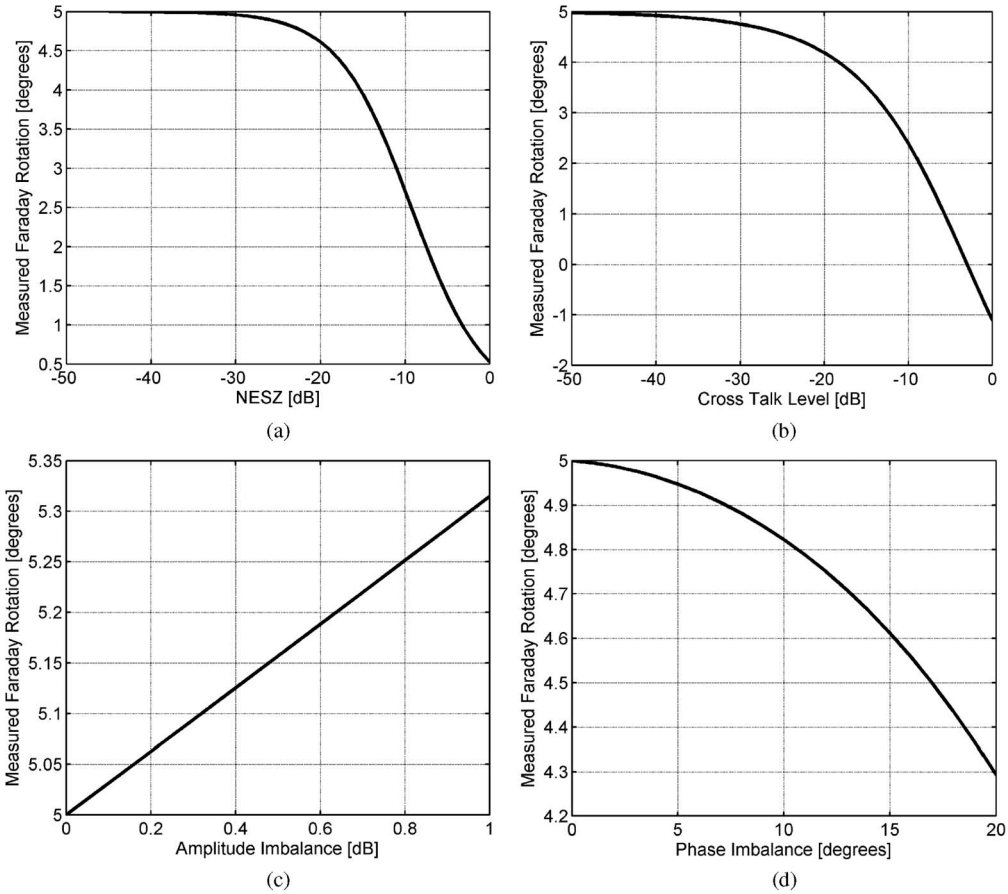

Fig. 3. Biases of $\hat{\Omega}$ due to (a) noise influence, (b) crosstalk, (c) amplitude imbalance, and (d) phase imbalance. "Bare soil" surface type is used to exemplify the effects. The real FR is assumed to be $\Omega = 5^\circ$.

An analysis of Fig. 2 yields the following.

1) FR estimates $\hat{\Omega}$ within a SAR scene may be biased by up to 4°, depending on the true FR, the calibration quality, and the surface type.
2) In heterogeneous areas, FR biases may vary spatially by up to 1.7°, causing a spread of the statistical distribution of FR estimates throughout a SAR image.
3) In the presence of calibration errors, bias and standard deviation of FR estimation are *dependent on the magnitude* of the (true) FR in a nonlinear fashion and generally *increase with* Ω.

These findings have to be kept in mind when analyzing the FR estimation results in Section III-B.

In Fig. 3, the influence of the calibration-error system noise [Fig. 3(a)], crosstalk [Fig. 3(b)], amplitude imbalance [Fig. 3(c)], and phase imbalance [Fig. 3(d)] on $\hat{\Omega}$ is analyzed individually. "Bare soil" surface type is used to exemplify the effects, and a real FR of $\Omega = 5^\circ$ is assumed. Residual system noise generally causes a bias of FR estimates toward zero. The magnitude of the bias increases with decreasing signal-to-noise (SNR) ratio. Noise-induced biases can be modeled if both the system noise and the (average) scattering signature of the observed surface are known. Residual crosstalk creates apparent FR rotation, resulting in a bias of $\hat{\Omega}$ increasing with crosstalk level [see Fig. 3(b)]. The influence of amplitude and phase imbalances on $\hat{\Omega}$ is less dramatic. All effects scale with Ω and are less pronounced for low Ω.

III. FR IN ALOS PALSAR DATA

A. Predicted FR in ALOS PALSAR Data

By using the prediction approach presented in Section II-B, the AADN ALOS PALSAR archive at ASF has been screened for images with high FR. While there are many thousands of images available in the archive, there are only a few fully polarimetric images with a predicted FR larger than 3°, all contained in a handful of acquisitions. The low number of affected images stems from the fact that current TEC values are at a minimum in the 11-year solar cycle, and most PALSAR acquisitions occur at a local time of 2200, when TEC activity is typically low.

In Fig. 4, latitude-dependent trends of predicted FR are shown. The dots represent the FR predictions obtained using (6) for SAR data holdings at AADN as of January 23, 2007. From Fig. 4, we see that the most extreme FR angles are not expected at the equator. At equatorial latitudes, the TEC values are highest, but the magnetic field is largely perpendicular to the pointing angle, with perpendicular orientation occurring at the geomagnetic equator. At polar latitudes, the magnetic field vector is much more aligned with the satellite pointing angle, but TEC values tend to be low. At intermediate latitudes (between 30° and 50°), moderately high TEC values and a magnetic field that is more aligned with the imaging direction yield the largest expected FR (cf. Fig. 4). Since the geomagnetic equator is located 10° south of the physical equator, minimal FR angles are observed at 10° south for the Americas.

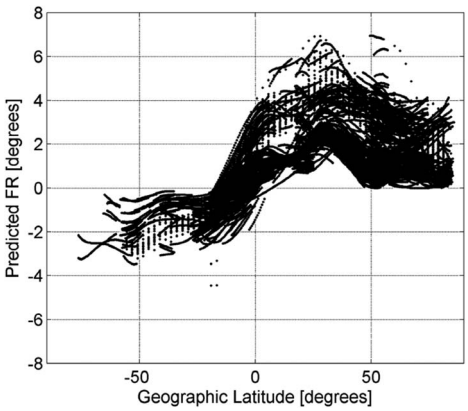

Fig. 4. Predicted FR as a function of latitude. Data shown are for all ALOS PALSAR holdings at AADN as of January 23, 2007. Predicted values are calculated using (6).

FR values are expected to increase during the lifetime of PALSAR due to an increasing solar activity until the year 2011. In [8], a generic model with similar satellite parameters to those used for ALOS predicts FR values from 0° to 7° for low solar activity (assuming solar minimum around 2007) and values from 0° to 27° for high solar activity. The results for solar minimum are in good agreement with the prediction values shown in Fig. 4, which are stemming from a comparable time period.

Although the prediction has been proven useful, it is limited by the precision of the model, particularly by the spatial and temporal resolutions of the vertical TEC maps. As will be shown in Section III-B, the FR within a PALSAR image can vary dramatically, while the corresponding GIM shows little or no change in TEC. This represents not an error in the TEC but a lack of resolution, both spatial and temporal.

B. FR Estimation From PALSAR Data

The FR estimation is performed following the approach presented in (14) of Section II-C. In a first step, the complex SAR data are averaged over an area large enough to reduce speckle noise but small enough to retain possible low-frequency FR variations within the image. In our case, a box car filter of 10×10 pixels was chosen. In a second step, estimates $\hat{\Omega}$ of the real FR Ω are derived from the averaged data by applying (13) and (14). The following examples illustrate the results.

Fig. 5 shows an example of FR estimation for a full-pol PALSAR data set over Delta Junction, Alaska. The left panel of Fig. 5 corresponds to the intensity of the "circular cross-pol product" abs$(Z_{12}Z_{21}^*)$ from (14). The center panel shows the spatial distribution of FR estimates $\hat{\Omega}$. The right panel is split into three tiles, each of which displays basic statistical measures. The top tile shows the statistical distribution of $\hat{\Omega}$, including an estimate for the average FR $(\mu_{\hat{\Omega}})$ and its standard deviation $(\sigma_{\hat{\Omega}})$. The center tile shows trends over range, while azimuth trends are presented in the lower tile.

The estimated FR in the Delta Junction example is relatively constant across the image with a mean value of $\mu_{\hat{\Omega}} = -0.1°$, estimated with an accuracy of $\sigma_{\hat{\Omega}} = 0.11°$. Besides the low $\sigma_{\hat{\Omega}}$, the spatial stability of the FR estimate (center panel of Fig. 5) indicates the high quality of the estimation procedure. Although no significant FR was present in this case, it still exhibits some

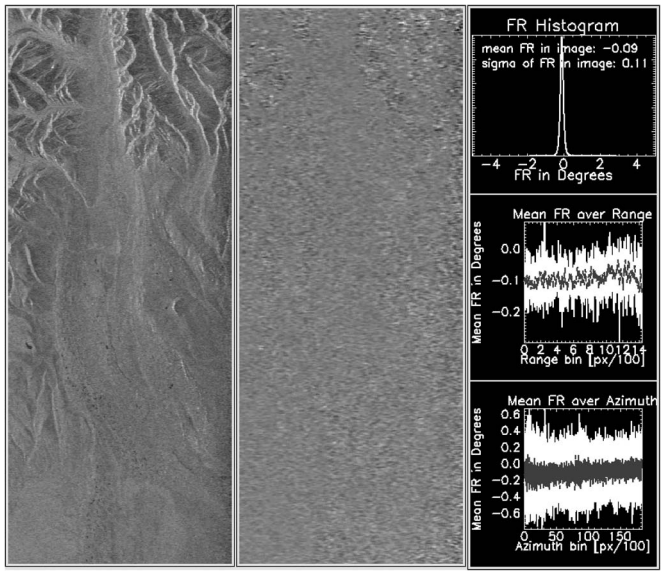

Fig. 5. Example of FR estimation from quad-polarimetric PALSAR data over the area of Delta Junction, Alaska. The left panel corresponds to the intensity of the circular cross-pol product (abs$(Z_{12}Z_{21}^*)$). The FR estimates $\hat{\Omega}$ are shown in the center. Statistical plots, as well as range and azimuth trends, are presented in the right.

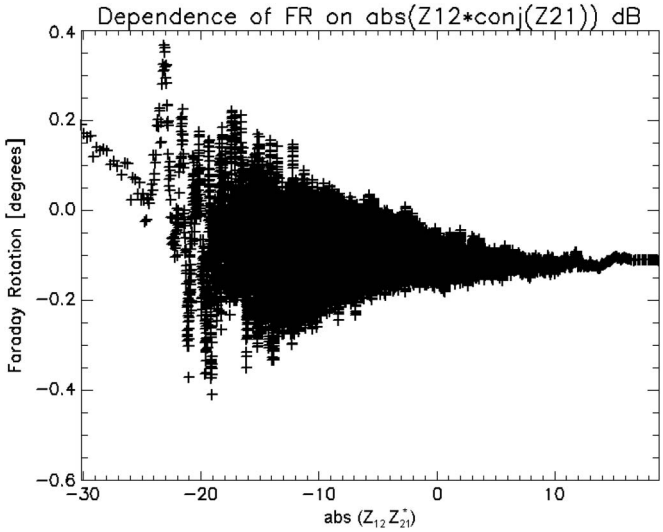

Fig. 6. FR estimates as a function of signal amplitude. The increase of noise with decreasing SNR ratio is clearly visible.

features worth mentioning. A closer look at the right panel in Fig. 5 suggests a normal distribution of $\hat{\Omega}$ with $\sigma_{\hat{\Omega}}$ dominated by thermal noise and remaining speckle, which were not fully removed by the 10×10 averaging. This is proven in Fig. 6 where the FR estimates are plotted versus abs$(Z_{12}Z_{21}^*)$. The increased variance with a decreasing abs$(Z_{12}Z_{21}^*)$ is clearly visible, stemming from the increasing influence of thermal noise. By considering the low $\mu_{\hat{\Omega}}$, an increase of $\sigma_{\hat{\Omega}}$ due to target-dependent FR biases is not expected (cf. Fig. 2).

Fig. 7(a) shows the FR estimation results of a full-pol PALSAR image acquired over Fairbanks, Alaska. An average FR of $\mu_{\hat{\Omega}} = 1.95°$ was estimated with a standard deviation of $\sigma_{\hat{\Omega}} = 0.16°$. $\hat{\Omega}$ is statistically significant. The spatial stability of the FR estimate is again obvious, and no pronounced trends over range and azimuth can be observed. Fig. 7(b) shows

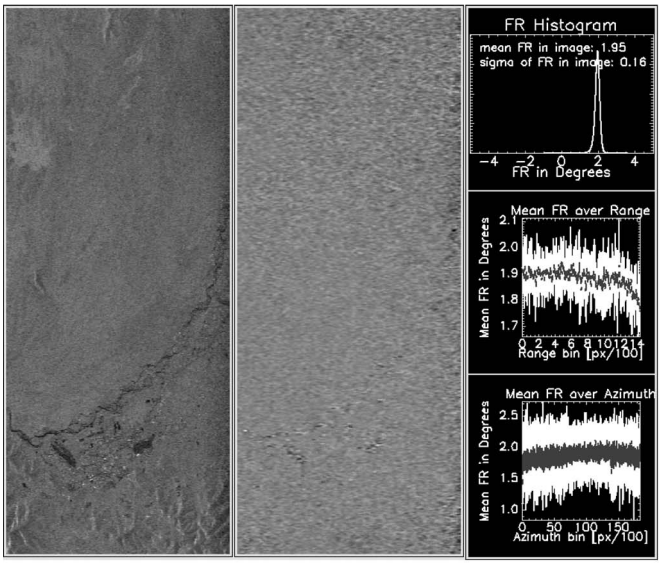

(a)

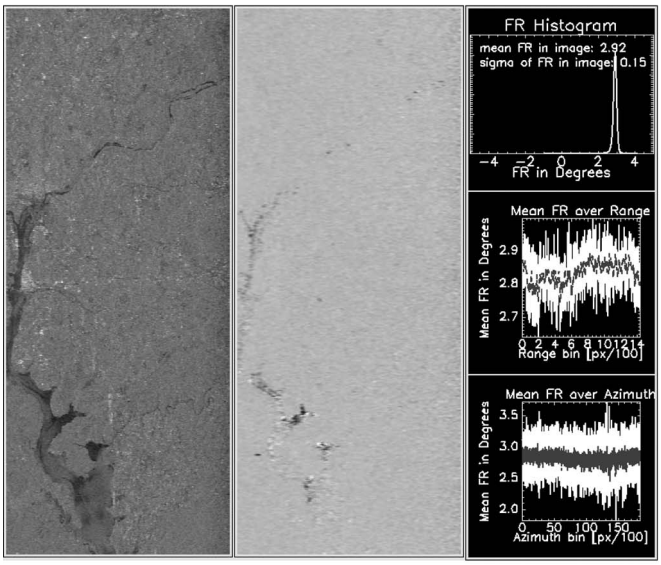

(b)

Fig. 7. (a) Example of FR estimation from a full-pol PALSAR data set over the area of Fairbanks, Alaska. (b) FR estimation for an ALOS PALSAR image located near Washington, DC.

similar results for an area around Washington, DC. The average FR was estimated to be $\mu_{\hat{\Omega}} = 2.92^\circ$ with a standard deviation of $\sigma_{\hat{\Omega}} = 0.15^\circ$. The FR appears to be quite stable throughout the image, although some artifacts are evident. The artifacts are coincident with areas of low backscatter in the intensity image and are discussed in more detail in Section III-C.

The last example, shown in Fig. 8, illustrates a case where significant variations of FR within the spatial extent of a PALSAR image are evident. The histogram of $\hat{\Omega}$ indicates three different ionospheric regimes with mean values between $\mu_{\hat{\Omega}} = 3^\circ$ and $\mu_{\hat{\Omega}} = 4^\circ$. Significant range and azimuth structure is evident, with an azimuth variation of $\hat{\Omega}$ of more than 2° across the image. The image is located in the vicinity of the magnetic north pole, and the variations visible in the image are to a major extent caused by fluctuations in the number of free electrons in the ionosphere.

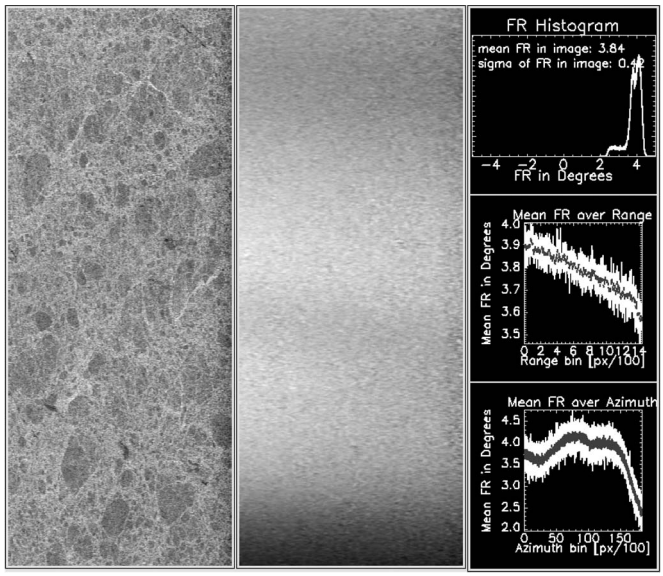

Fig. 8. Example of FR estimation for an area close to the geomagnetic North Pole. FR trends in range and azimuth are evident.

C. Experiences With Noise-Induced Estimation Biases

The FR estimates shown in Fig. 7(a) and (b) appear to be spatially stable yet show some artifacts that coincide with areas of low backscatter in their corresponding intensity images. Plotting the FR estimates of Fig. 7(a) and (b) versus the intensity of the respective circular cross-pol products results in the graphs in Fig. 9(a) and (b). Besides the intensity dependence of $\sigma_{\hat{\Omega}}$, which was already observed in Fig. 6, a bias of the FR estimates is evident, whose size increases with decreasing signal brightness. This noise-induced bias is predicted in Section II-C2, and its dependence on the noise level is shown in Fig. 3(a).

The theoretical bias of $\hat{\Omega}$ can be derived from (9) if both the system noise matrix and the surface scattering characteristics are known. If the surface scattering is not known, the bias can be approximated by normalizing the image and replacing NESZ with the average SNR ratio. This simplification has been used to approximate the theoretical biases of $\hat{\Omega}$ in the analyzed SAR data. Examples of these approximations are represented by gray lines in Fig. 9(a) and (b). A NESZ of -27 dB is assumed for the calculations. The match with the measurements is striking and confirms the theory. The gray lines represent the *average* noise-induced FR bias. Deviations from the line are caused by residual speckle noise and by residual crosstalk and channel imbalance.

An analysis of the data acquired near the geomagnetic North Pole (see Fig. 8) is shown in Fig. 10. The dependence of the estimated FR on SNR causes a bias of $\hat{\Omega}$ for low signal levels. In addition, the variation of FR throughout the image leads to an increased spread of data points.

D. Validation of FR Estimates

In addition to the data sets analyzed in detail in the previous section, FR angles were estimated for 20 other full-pol PALSAR scenes. A least squares linear fit between the FR prediction and the FR estimation yields a slope of

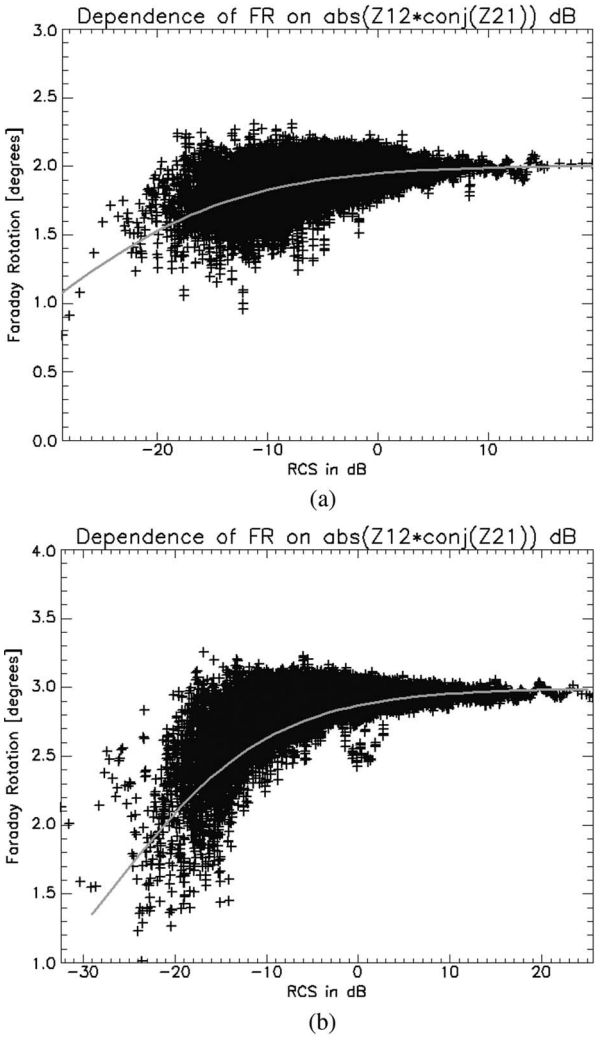

Fig. 9. FR estimates as a function of signal amplitude for (a) Fairbanks, Alaska and (b) Washington, DC. The SNR-dependent bias introduced by correlated noise is indicated by a gray line.

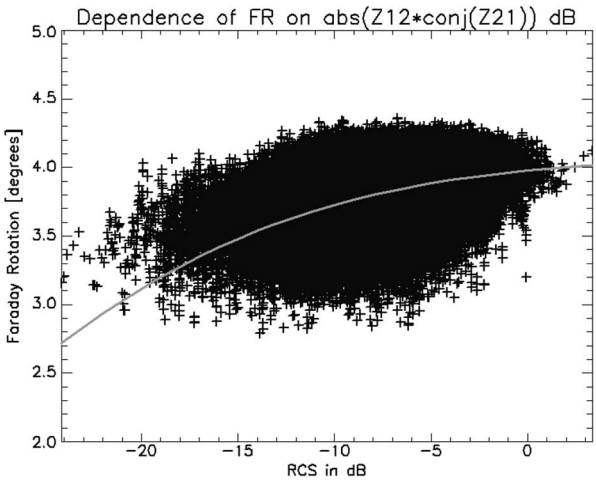

Fig. 10. FR estimates as a function of signal amplitude. The increase of noise with decreasing SNR ratio is evident.

$m = 1.09(\sigma_m = 0.09)$ and an intercept of $b = 0.5(\sigma_b = 0.2)$. The correlation between the two data sets is shown in Fig. 11 where the y-axis represents prediction and the x-axis represents estimated FR.

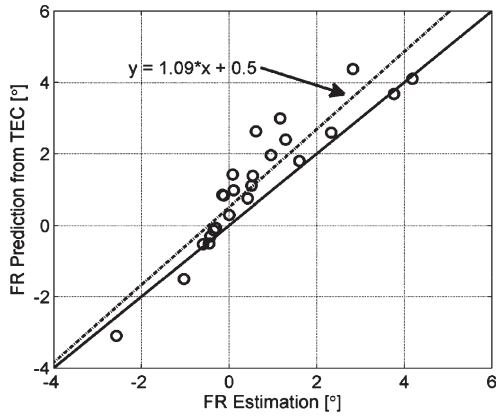

Fig. 11. FR predicted from TEC [(6)] and estimated from data [(13) and (14)] to 24 fully polarimetric PALSAR acquisitions. Dashed line is the least squares fit to the data. Solid line is the ideal.

While the prediction agrees reasonably well with estimates, there are limitations to the precision of the fit. There are few points in the curve at the extremes of the fit, which significantly affect the determination of the slope. The available data characterize a very small region (-3° to 5°) of the possible FR values ($\sim -25^\circ$ to $\sim 25^\circ$); thus, caution is advised when extrapolating the correlation to a much higher FR.

The deviation of the slope from $m = 1.0$ can be explained by calibration errors in the analyzed PALSAR data. Based on Fig. 2, imperfect calibration causes an underestimation of FR in the northern hemisphere and an overestimation of FR south of the geomagnetic equator. The slope bias shown in Fig. 11 is consistent with theoretical biases introduced by the range of residual calibration errors mentioned in Section II-C. The origin of the intercept bias is most probably introduced by the uneven distribution of samples used for defining the linear trend. Additional observations, particularly with larger FR, are needed for a more robust analysis of FR biases and for a more in-depth assertion of the nature and size of calibration errors.

IV. Correction for FR

A correction of full-pol SAR data for FR can be performed by inverting the equation system in (10) resulting in [16]

$$\begin{bmatrix} \widetilde{S}_{\mathrm{hh}} & \widetilde{S}_{\mathrm{vh}} \\ \widetilde{S}_{\mathrm{hv}} & \widetilde{S}_{\mathrm{vv}} \end{bmatrix} = \begin{bmatrix} \cos\Omega & -\sin\Omega \\ \sin\Omega & \cos\Omega \end{bmatrix} \cdot \begin{bmatrix} M'_{\mathrm{hh}} & M'_{\mathrm{vh}} \\ M'_{\mathrm{hv}} & M'_{\mathrm{vv}} \end{bmatrix} \cdot \begin{bmatrix} \cos\Omega & -\sin\Omega \\ \sin\Omega & \cos\Omega \end{bmatrix}. \quad (15)$$

To derive an unbiased approximation $\widetilde{S}$ of the correct scattering matrix S, unbiased FR angles have to be used for FR correction. Based on the findings in Section III, the following four different cases have to be distinguished.

A. Case I: Spatially Constant FR and High SNR

SNR values higher than 10 dB allow the estimation of FR with a bias of less than 10%. If a NESZ of -27 dB is assumed, a signal level of -17 dB is required. Three options for deriving unbiased FR values $\overline{\Omega}$ are proposed as follows.

If the SNR is high across the image, unbiased FR angles can be derived with high accuracy by averaging the initial FR estimates over the entire image. FR biases can be ignored.

If the SNR varies significantly within the image, unbiased estimates of FR can be derived by either masking the image and estimating $\hat{\Omega}$ from bright areas only or by correcting biased FR estimates according to the local SNR. Note that a correction of $\hat{\Omega}$ according to the local SNR is only an approximation. The Washington, DC image of Fig. 7(b) serves as an example for this correction scenario. For this data set, both a spatially constant ionospheric activity and a generally high SNR were observed. To correct the data, areas darker than -10 dB were masked out, and an estimate of the unbiased FR angle $\overline{\Omega}$ was derived by averaging $\hat{\Omega}$ over the remaining parts of the image. Fig. 12 shows the results of the correction procedure. The left panel in Fig. 12(a) shows the intensity of $(M'_{\mathrm{vh}} - M'_{\mathrm{hv}})$ before FR correction. $(M'_{\mathrm{vh}} - M'_{\mathrm{hv}})$, which is supposed to be zero if $\Omega = 0^\circ$, shows significant structure. The center panel of Fig. 12(a) shows $(\widetilde{S}_{\mathrm{vh}} - \widetilde{S}_{\mathrm{hv}})$. After FR correction, the structure vanishes almost completely, indicating a successful FR correction. The statistical plots on the right side of Fig. 12(a) show the residual FR in the corrected data, which appears to be statistically insignificant.

In Fig. 12(b), the remaining FR is plotted as a function of $\mathrm{abs}(Z_{12}Z_{21}^*)$. It indicates the perfect removal of the original 3° FR for all pixels with SNR ≥ 10 dB. In areas of SNR < 10 dB, FR appears to be overcompensated. Note that this bias is not created by the signal but by the noise component in the data, which has an *a posteriori* FR of $\dot{\Omega} = 2.92^\circ$. The histogram of $\mathrm{abs}(Z_{12}Z_{21}^*)$ in Fig. 12(b) shows that only a small fraction of image pixels is affected by significant FR biases.

B. Case II: Spatially Constant FR and Low SNR

If the signal amplitude is low across the entire image, most of the FR estimates will be biased. From knowing the SNR and the noise level of the data, local FR biases can be estimated from (9), and unbiased FR angles $\overline{\Omega}$ can be approximated. A subsequent correction by $\overline{\Omega}$ can be performed. If the bright patches exist in the image, a threshold can be applied, and $\overline{\Omega}$ can be estimated by averaging $\hat{\Omega}$ over these areas. No data set of our collection fits these conditions.

C. Case III: Spatially Varying FR and High SNR

The physically correct FR is derived by fitting an adaptive polynomial plane to the $\hat{\Omega}$ estimates. If patches with significant bias are identified, we recommend masking the data before fitting to avoid mixing spatially varying ionospheric activity with noise dependence. For fitting, an iterative least squares algorithm combined with a parameter significance test is used. At first, a polynomial surface of high order is fitted to the data. The fitting is followed by a significance test of the parameters of the polynomial surface. Insignificant parameters are removed from the model, and a reduced model is used in the second iteration. No data set of our collection fits these conditions.

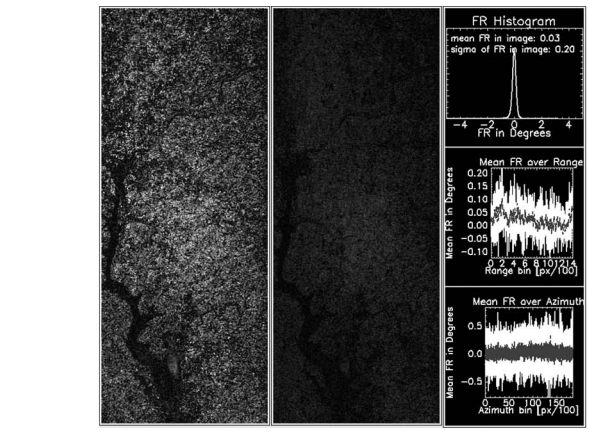

(a)

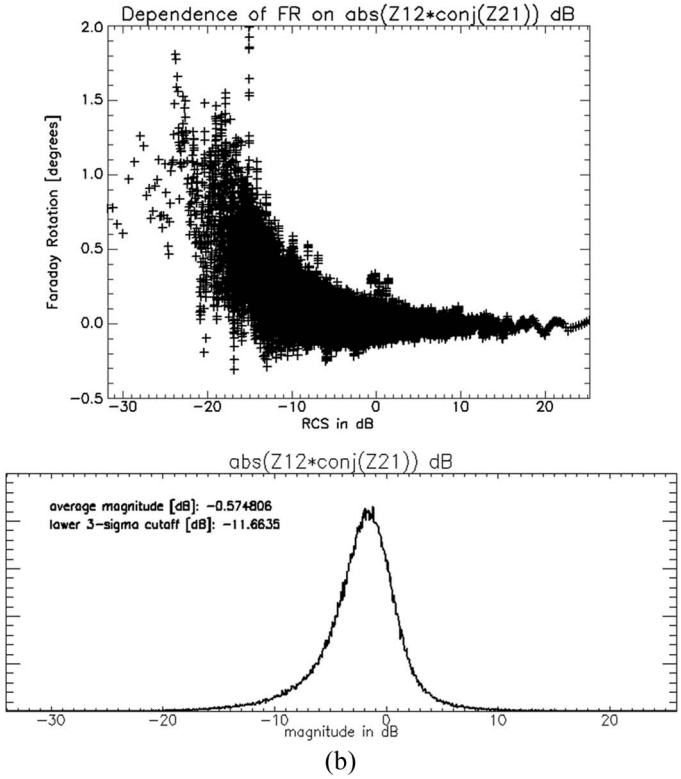

(b)

Fig. 12. (a) Control of FR correction. Left panel: Magnitude of $(M'_{\mathrm{vh}} - M'_{\mathrm{hv}})$. Center panel: Magnitude of $(\widetilde{S}_{\mathrm{vh}} - \widetilde{S}_{\mathrm{hv}})$. Right tiles: (Top) Remaining FR after correction. Center and lower tiles: Range and azimuth dependence of remaining FR. (b) Dependence of remaining FR on signal intensity together with a histogram of $\mathrm{abs}(Z_{12}Z_{21}^*)^2$.

D. Case IV: Spatially Varying FR and Low SNR

In this case, most of the FR estimates across the image suffer from biases, and a separation of noise-induced variation of $\hat{\Omega}$ and spatial variation of ionospheric activity is difficult. A selection of a subset of spatially distributed bright pixels is an option to reduce bias while retaining the ability to estimate the spatial variation of FR. The example in Fig. 8 is used to exemplify this approach. From the original data set, only pixels of SNR ≥ 10 dB are selected by thresholding. A polynomial plane is fitted to the remaining pixels using an iterative least squares adjustment. Fig. 13(a) shows the original data set along with the estimated polynomial plane. The correction results are shown in Fig. 13(b). The remaining FR angle after correction is

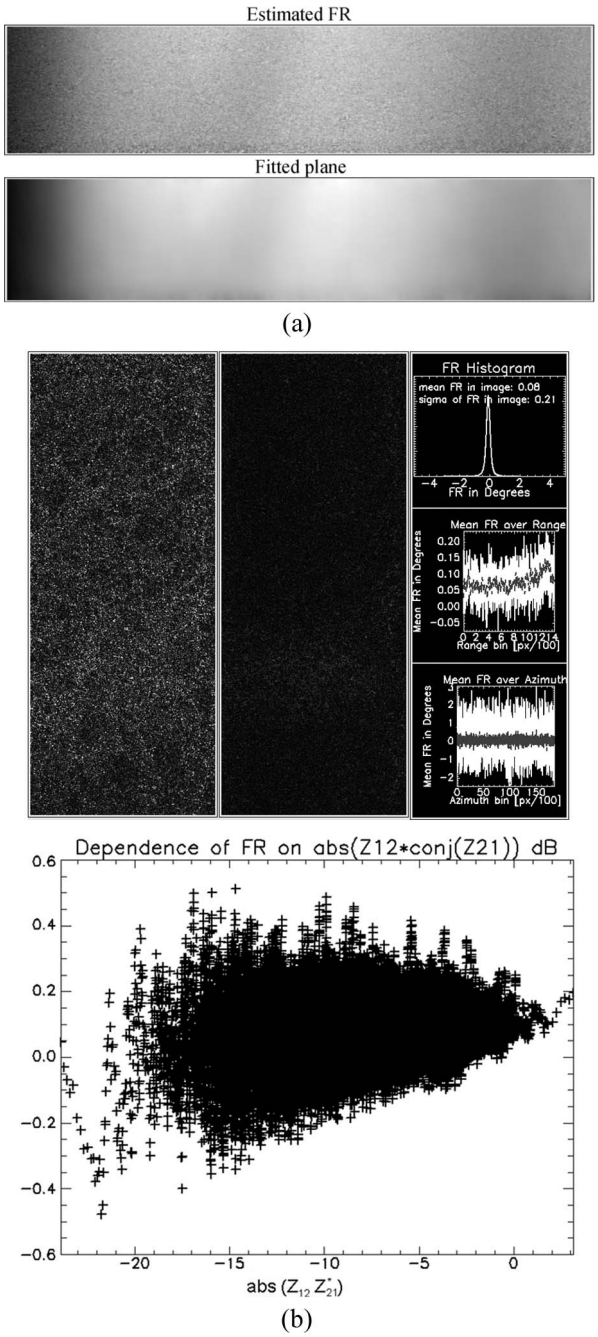

Fig. 13. FR correction of the example in Fig. 8. (a) Spatial fit to varying FR in Fig. 8. (b) Analysis of the residual FR after FR correction (top) together with the dependence of residual FR on signal intensity (bottom).

about -0.01° and not significant. For high SNR, the FR seems to be undercompensated by about 0.01°. A remaining slope is visible in the plot. We do not recommend a local correction of FR biases, as the uncertainties introduced by this method may mask the spatial variability of TEC.

V. Performance Discussion

The main limitations of FR estimation and correction are the consequences of imperfect data calibration, limited data availability, estimation biases, and noise in the FR estimator.

Equation (9), as well as error analyses in Section II-B2, indicates that the quality of data calibration is limiting the precision and accuracy of FR estimation. Residual noise, channel imbalance, and crosstalk cause biases and spatial variability in the estimated FR angles that increase with Ω. The nature and size of these effects, as expected for ALOS PALSAR, are described and quantified in Section II-B2. More background information on error sources in FR estimation can also be found in, e.g., [16].

FR correction is particularly important for dual- and full-pol data sets, as they are used for polarimetric analyses. Current FR correction methods require full-pol imagery to successfully estimate and remove FR effects from the data. An analysis of the ALOS PALSAR archive of the AADN revealed, however, that only about 10% of all archived data takes are acquired in a full-pol mode. Even though a correction of dual-pol images may be possible for $\Omega \leq 10^\circ$ (see [20]), correction of FR effects is not possible for a substantial part of the archive. Therefore, the applicability of PALSAR data to polarimetric applications may be reduced at times of high ionospheric activity. FR effects on single-pol amplitudes are moderate as long as $\Omega \leq 20^\circ$. A detailed study of FR effects on L-band backscatter amplitudes is published in [10].

FR effects and calibration parameters like crosstalk and channel imbalance are hard to distinguish, as they cause similar effects in uncalibrated SAR data. If established methods for calibrating full-pol SAR data are applied (e.g., [16], [21], and [22]), the presence of unknown FR complicates the determination of calibration parameters and, therefore, limits the achievable calibration quality. FR prediction, as presented in Section II-B, may support the determination of calibration parameters by providing *a priori* information about ionospheric distortions. By considering the analyses in Sections II-B2 and C2, the benefit of predicted FR for limiting SAR calibration errors can be estimated. Assume, for example, that the real FR in SAR data acquired at a calibration site (e.g., rain forest) is $\Omega = 10^\circ$. If TEC maps allow the prediction of the real FR with an accuracy of 0.5° and the predicted values are applied in the calibration procedure, crosstalk ($|\delta|^2$), amplitude imbalance ($|f|^2$), and phase imbalance ($\arg(f)$) calibration errors can be limited to $\sigma_{|\delta|^2} \approx -30$ dB, $\sigma_{|f|^2} \approx 0.8$ dB, and $\sigma_{\arg(f)} \approx 12^\circ$. In addition, FR prediction supports a careful selection of calibration data sets by limiting ionospheric influence.

FR introduces some effects that are irreversible without additional knowledge. Two images affected by significantly different FR will observe the ground with different polarization and, thus, "see" different aspects of the same surface. Interferometric pairs formed from such images will suffer from a decrease of coherence and may show a differential interferometric phase induced by different surface penetration. More information on this topic can be found in [23].

VI. Conclusion and Outlook

FR has the potential to significantly affect the ALOS PALSAR data. In the Americas, the largest effects are expected in areas about 30° north and 50° south of the equator. This paper

proves that the detection and correction of FR is feasible with high accuracy. A set of real data examples shows the quality and sensitivity of FR estimation from the PALSAR data, allowing the measurement of FR with high precision in areas where such measurements were previously inaccessible. An error analysis concluded that calibration errors introduce surface-type-dependent biases into FR estimation that scale nonlinearly with Ω. It is shown that the high calibration quality of PALSAR minimizes the impact of these effects. Careful data analysis and handling allows the mitigation of FR biases in many cases. In examples, the detection of kilometer-scale ionospheric disturbances, a spatial scale that is not detectable in ground-based GPS measurements, was presented. Globally available TEC maps, derived from GPS observations, are suitable to predict FR angles in SAR data with an accuracy of less than 1°, if sufficient spatial sampling of the true ionospheric signal can be assumed. With increasing solar activity in upcoming years, observed FR angles will be larger, and concomitant imaging effects will be more egregious.

ACKNOWLEDGMENT

The authors would like to thank the PALSAR team for providing high-quality data that made this paper possible. The authors would also like to thank Dr. A. Freeman and Dr. T. Ainsworth for their input and many fruitful discussions.

REFERENCES

[1] Z.-W. Xu, J. Wu, and Z.-S. Wu, "A survey of ionospheric effects on space-based radar," *Waves Random Media*, vol. 14, no. 2, pp. S189–S273, Apr. 2004.

[2] F. Meyer, R. Bamler, N. Jakowski, and T. Fritz, "The potential of low-frequency SAR systems for mapping ionospheric TEC distributions," *IEEE Geosci. Remote Sens. Lett.*, vol. 3, no. 4, pp. 560–564, Oct. 2006.

[3] U. Wegmueller, C. Werner, T. Strozzi, and A. Wiesmann, "Ionospheric electron concentration effects on SAR and INSAR," in *Proc. IGARSS*, Denver, CO, 2006, pp. 3731–3734.

[4] A. L. Gray and K. E. Mattar, "Influence of ionospheric electron density fluctuations on satellite radar interferometry," *Geophys. Res. Lett.*, vol. 27, no. 10, pp. 1451–1454, May 2000.

[5] L. Li and F. Li, "SAR imaging degradation by ionospheric irregularities based on TFTPCF analysis," *IEEE Trans. Geosci. Remote Sens.*, vol. 45, no. 5, pp. 1123–1130, May 2007.

[6] J. Liu, Y. Kuga, A. Ishimaru, X. Pi, and A. Freeman, "Ionospheric effects on SAR imaging: A numerical study," *IEEE Trans. Geosci. Remote Sens.*, vol. 41, no. 5, pp. 939–947, May 2003.

[7] A. R. Thompson, J. M. Moran, and G. W. Swenson, *Interferometry and Synthesis in Radar Astronomy*. New York: Wiley, 1986.

[8] P. A. Wright, S. Quegan, N. S. Wheadon, and C. D. Hall, "Faraday rotation effects on L-band spaceborne SAR data," *IEEE Trans. Geosci. Remote Sens.*, vol. 41, no. 12, pp. 2735–2744, Dec. 2003.

[9] R.-Y. Qi and Y.-Q. Jin, "Analysis of the effects of Faraday rotation on spaceborne polarimetric SAR observations at P-band," *IEEE Trans. Geosci. Remote Sens.*, vol. 45, no. 5, pp. 1115–1122, May 2007.

[10] A. Freeman and S. Saatchi, "On the detection of Faraday rotation in linearly polarized L-band SAR backscatter signatures," *IEEE Trans. Geosci. Remote Sens.*, vol. 42, no. 8, pp. 1607–1616, Aug. 2004.

[11] B. K. Banerjea, "On the propagation of electromagnetic waves through the atmosphere," *Proc. R. Soc. Lond. A, Math. Phys. Sci.*, vol. 190, no. 1020, pp. 67–81, Jun. 1947.

[12] S. Schaer, "Mapping and predicting the Earth's ionosphere using the Global Positioning System," Ph.D. dissertation, Geodätisch-Geophysikalische Arbeiten der Schweiz, vol. 59, Schweizerische Geodaetische Kommission, Zuerich, 1999. ISBN 3-908440-01-7.

[13] M. Hernandez-Pajares, "IGS ionosphere WG status report: Performance of IGS ionosphere TEC maps," in *Proc. IGS Workshop 'Celebrating a Decade of the International GPS Service'*, 2004, pp. 225–237.

[14] G. A. Hajj, L. C. Lee, X. Pi, L. J. Romans, W. S. Schreiner, P. R. Straus, and C. Wang, "COSMIC GPS ionospheric sensing and space weather," *Terrestrial, Atmospheric Ocean. Sci.*, vol. 11, no. 1, pp. 235–272, 2000.

[15] S. McLean, S. Macmillan, S. Maus, V. Lesur, A. Thomson, and D. Dater, "The US/UK world magnetic model for 2005–2010," NOAA Tech. Rep. NESDIS/NGDC-1, Dec. 2004. [Online]. Available: http://www.ngdc.noaa.gov/geomag/WMM/data/TRWMM2005.pdf

[16] A. Freeman, "Calibration of linearly polarized polarimetric SAR data subject to Faraday rotation," *IEEE Trans. Geosci. Remote Sens.*, vol. 42, no. 8, pp. 1617–1624, Aug. 2004.

[17] T. Boerner, K. P. Papathanassiou, N. Marquart, M. Zink, M. Meininger, P. J. Meadows, A. J. Rye, P. Wright, and B. Rosich Tell, "ALOS PALSAR products verification," in *Proc. IGARSS*, Barcelona, Spain, 2007, pp. 5214–5217.

[18] L. E. B. Eriksson, G. Sandberg, L. M. H. Ulander, G. Smith-Jonforsen, B. Hallberg, K. Folkesson, J. E. S. Fransson, M. Magnusson, and H. Olsson, "ALOS PALSAR calibration and validation results from Sweden," in *Proc. IGARSS*, Barcelona, Spain, 2007, pp. 1589–1592.

[19] S. H. Bickel and R. H. T. Bates, "Effects of magneto-ionic propagation on the polarization scattering matrix," *Proc. IEEE*, vol. 53, no. 8, pp. 1089–1091, Aug. 1965.

[20] J. Nicoll and F. Meyer, "Mapping the ionosphere using L-band SAR data," in *Proc. IGARSS08*, Boston, MA, 2008, to be published.

[21] S. Quegan, "A unified algorithm for phase and cross-talk calibration of polarimetric data—Theory and observations," *IEEE Trans. Geosci. Remote Sens.*, vol. 32, no. 1, pp. 89–99, Jan. 1994.

[22] J. J. van Zyl, "Calibration of polarimetric radar images using only image parameters and trihedral corner reflector responses," *IEEE Trans. Geosci. Remote Sens.*, vol. 28, no. 3, pp. 337–348, May 1990.

[23] E. J. M. Rignot, "Effect of Faraday rotation on L-band interferometric and polarimetric synthetic-aperture radar data," *IEEE Trans. Geosci. Remote Sens.*, vol. 38, no. 1, pp. 383–390, Jan. 2000.

Franz J. Meyer (S'03–A'03–M'04) received the Diploma degree in geodetic engineering and the Doctor of Engineering degree from the Technische Universitaet Muenchen, Munich, Germany, in 2000 and 2004, respectively.

From August 2000 to September 2003, he was with the Chair for Photogrammetry and Remote Sensing, Technische Universitaet Muenchen, where he mainly worked on SAR interferometry and differential SAR interferometry. From October 2003 to February 2007, he was a scientific employee with the Remote Sensing Technology Institute, German Aerospace Center, Oberpfaffenhofen, where his scientific work was focused on SAR interferometry techniques for current and future SAR satellites (e.g., TerraSAR-X and -L), the conception of algorithms for traffic monitoring using SAR satellites (e.g., TerraSAR-X), the correction and modeling of atmospheric effects in INSAR data, and persistent scatterer interferometry. Since March 2007, he has been a Research Scientist with the Alaska Satellite Facility, University of Alaska Fairbanks, Fairbanks. His current work includes studies of ionospheric effects on SAR, SAR interferometry applications, SAR processing, and SAR data quality analysis. He is the author of more than 50 scientific publications, including two being acknowledged as "Best Papers."

Jeremy B. Nicoll received the B.S. degree in chemistry and the M.S. degree in analytical chemistry from Brigham Young University, Provo, Utah, in 1995 and 1997, respectively.

Since 1998, he has been with Fairbanks' Geophysical Institute, Alaska Satellite Facility (ASF), University of Alaska Fairbanks, Fairbanks, AK. He was a Calibration Engineer, focusing on analytical and statistical approaches to product quality. In 2001, he became a Software Developer, working on signal-processing algorithms related to SAR, with emphasis on saturation power-loss compensation. In 2003, he was appointed Lead of ASF's Technical Services Office. In 2004, he became the Engineering Center Manager, overseeing the hardware and infrastructure software at ASF. His research interests include Faraday rotation and ionospheric effects in SAR data.